

Spatial filtering of interfering signals at the initial Low Frequency Array (LOFAR) phased array test station

A. J. Boonstra

Research and Development Department, Netherlands Foundation for Research in Astronomy, Dwingeloo, Netherlands

S. van der Tol

Department of Electrical Engineering, Delft University of Technology, Delft, Netherlands

Received 26 July 2004; revised 28 November 2004; accepted 2 March 2005; published XX Month 2005.

[1] The Low Frequency Array (LOFAR) is a radio telescope currently being designed. Its targeted observational frequency window lies in the range of 10–250 MHz. In frequency bands in which there is interference, the sensitivity of LOFAR can be enhanced by interference mitigation techniques. In this paper we demonstrate spatial filtering capabilities at the LOFAR initial test station (ITS) and relate it to the LOFAR radio frequency interference mitigation strategy. We show that in frequency ranges which are occupied with moderate-intensity man-made radio signals, the strongest observed astronomical sky sources can be recovered by spatial filtering. We also show that under certain conditions, intermodulation products of point-like interfering sources remain point sources. This means that intermodulation product filtering can be done in the same way as for “direct” interference. We further discuss some of the ITS system properties such as cross-talk and sky noise limited observations. Finally, we demonstrate the use of several beam former types for ITS.

Citation: Boonstra, A. J., and S. van der Tol (2005), Spatial filtering of interfering signals at the initial Low Frequency Array (LOFAR) phased array test station, *Radio Sci.*, 40, RS5S09, doi:10.1029/2004RS003135.

1. Introduction

1.1. Low Frequency Array Interference Mitigation

[2] The Low Frequency Array (LOFAR) is a next generation radio telescope which is currently being designed and which will be located in the Netherlands. LOFAR [Bregman, 2000] is an aperture array telescope [Thompson *et al.*, 1986; Raimond and Genee, 1996] and will consist of order 100 telescopes (stations), spread in spirals over an area of about 360 km, as well as in a more densely occupied central core. The observational frequency window will lie in the 10–250 MHz range. Each of the stations will consist of order 100 phased array antennae. These antennae are sky noise limited, and are combined in such a way that station beams can be formed for each of the desired station observing directions or pointings. The preliminary LOFAR design defines multiple beam capabilities, (noncontiguous)

4 MHz wide bands, and a frequency resolution of 44 1 kHz. The LOFAR initial operations phase is scheduled 45 to start in 2006; the target date to have LOFAR fully 46 operational is 2008. 47

[3] For testing and demonstration purposes, several 48 prototype stations are defined. One of these demonstra- 49 tors is the initial test station (ITS). It is a full-scale 50 prototype of a LOFAR station, and it became operational 51 in December 2003. ITS consists of 60 sky noise limited 52 dipoles, configured in a five-armed spiral, connected to a 53 digital receiver back end. ITS operates in the frequency 54 band 10–40 MHz, and the observed signals are directly 55 digitized without the use of mixers. The data can be 56 stored either as time series or as covariance matrices. 57

[4] In spectrum bands which are occupied with man- 58 made radio signals with moderate signal powers, the 59 unwanted man-made radio signals can be suppressed by 60 applying filtering techniques. In this paper we demon- 61 strate spatial filtering capabilities at the LOFAR ITS test 62 station, and relate it to the LOFAR radio frequency 63 interference (RFI) mitigation strategy [Boonstra, 2002]. 64 We show the effect of these spatial filters by applying 65

66 them to antenna covariance matrices, and by applying
 67 different beam-forming scenarios. We show that for
 68 moderate-intensity interferers (electric field strength \leq
 69 $0 \text{ dB}\mu\text{Vm}^{-1}$), the strongest observed astronomical sky
 70 sources can be recovered by spatial filtering. We also
 71 show that, under certain conditions, intermodulation
 72 products of point-like interfering sources remain point
 73 sources. This means that intermodulation product filter-
 74 ing can be done in the same way as for “direct”
 75 interference. We further discuss some of the ITS system
 76 properties such as cross talk and sky noise limited
 77 observations. Finally, we demonstrate the use of several
 78 beam former types for ITS.

80 1.2. Notation

81 [5] In this paper, scalars are denoted by nonbold
 82 lowercase and uppercase letters. Vectors are represented
 83 by bold lowercase letters, and matrices by uppercase
 84 bold letters. The hermitian conjugate transpose is
 85 denoted by $(\cdot)^H$, the transpose operator by $(\cdot)^t$, the
 86 expected value by $\mathcal{E}\{\cdot\}$, and the estimated values
 87 by $\hat{(\cdot)}$. The element-wise multiplication (Hadamard)
 88 matrix operator is denoted by \odot . For a vector $\mathbf{A} =$
 89 $(a_1, \dots, a_p)^t$, $e^{\mathbf{A}}$ is defined by $e^{\mathbf{A}} = (e^{a_1}, \dots, e^{a_p})^t$. \mathbf{I}
 90 represents the identity matrix, \mathbf{A}^{-1} denotes the matrix
 91 inverse of \mathbf{A} , and $\mathbf{A}^{\frac{1}{2}}$ denotes the matrix \mathbf{B} such that $\mathbf{B}^2 =$
 92 \mathbf{A} . Finally, $j = \sqrt{-1}$, $\mathbf{0}$ is the null matrix, the complex
 93 conjugate is denoted by $(\cdot)^*$, and $\text{diag}(\mathbf{A})$ converts the
 94 vector \mathbf{A} to a diagonal matrix with \mathbf{A} on the main
 95 diagonal.

97 2. LOFAR Interference Mitigation Strategy

98 [6] LOFAR will operate in bands where other spec-
 99 trum users are active, and in which interference may
 100 occur. However, it is expected that the sensitivity of
 101 LOFAR can be enhanced by applying filtering and
 102 interference mitigation techniques. In this way, parts of
 103 the bands occupied with moderate-intensity man-made
 104 radio signals, can be recovered for astronomical obser-
 105 vations. A description and results of some of the inter-
 106 ference mitigation techniques applied in radio astronomy
 107 can be found in work by *Briggs et al.* [2000], *Ellingson*
 108 *et al.* [2001], *Leshem and van der Veen*, [2000], *Leshem*
 109 *et al.* [2000], *Fridman and Baan* [2001], and *Barnbaum*
 110 *and Bradley* [1998].

111 2.1. Spectral Occupancy and LOFAR Sensitivity

112 [7] LOFAR will be one of the first radio telescopes in
 113 which RFI mitigation techniques will form an integral
 114 part of the system design. For several reasons, it was
 115 decided to equip LOFAR with relatively simple RFI
 116 mitigation techniques. In future phases of LOFAR, these
 117 techniques may be extended. A first constraint on com-

plexity is that the computing power required for inter- 118
 ference mitigation should be an order of magnitude less 119
 than what is required for the astronomical signal pro- 120
 cessing. Only in special cases is spending a major 121
 fraction of the computing resources on RFI mitigation 122
 acceptable. A second reason for relatively simple 123
 techniques is that the calibration of LOFAR [*Noordam*, 124
 2002, 2004] requires stable station beams. Only slowly 125
 varying (sidelobe) gains are allowed, otherwise the 126
 calibration process will not converge. For this reason, 127
 at station level, only spatial filters with fixed or slowly 128
 varying nulls are considered, as fast interference tracking 129
 would change the station beams too rapidly. A third 130
 reason is that interference mitigation is a relatively new 131
 field for radio astronomy, and that the effects of inter- 132
 ference mitigation related distortions are not in all cases 133
 quantified. 134

[8] The use of the radio spectrum in terms of signal 135
 power and time-frequency occupancy is roughly known 136
 from allocation tables and from monitoring observations. 137
 In order to estimate the required attenuation levels, the 138
 observed spectrum power needs to be related to the 139
 LOFAR sensitivity. One of the key parameters of 140
 the LOFAR aperture synthesis mode is that LOFAR will 141
 be sky noise dominated and its desired ultimate sensi- 142
 tivity will be a factor eight better than the thermal sky 143
 noise in a four hour full synthesis observation with order 144
 100 stations. *Kollen* [2004] specified a sensitivity of 145
 2 mJy ($1 \text{ Jy} = 10^{-26} \text{ W m}^2 \text{ Hz}^{-1}$) at 10 MHz down to 146
 0.03 mJy at 240 MHz for 1 hour integration over 4 MHz 147
 bandwidth, which corresponds to a 1 kHz bandwidth to 148
 127 mJy at 10 MHz down to 2.1 mJy at 240 MHz. In 149
 order to achieve this sensitivity and the required 150
 dynamic range, it is estimated that we need 4 MHz 151
 wide frequency bands for which we can recover 80% 152
 bandwidth. Here it is assumed that 20% bandwidth 153
 loss due to RFI does not lead to a dramatic decrease 154
 in sensitivity of the instrument as a whole. It is also 155
 assumed that in the 80% cleanest frequency bins 156
 within a 4 MHz band the RFI at station level is either 157
 at a 1–3 (station) sky noise sigma level, or can be 158
 reduced to this level by RFI mitigation techniques. The 159
 rationale of this is explained below. 160

162 2.2. Power Density Flux Levels

[9] The calibration capabilities of LOFAR [*Noordam*, 163
 2002] include the removal of strong sky sources such as 164
 Cas.A from the observed (uvw) data sets and images. 165
 This suggests that the remaining RFI can be removed in 166
 the same way as astronomical sources are removed, 167
 assuming that RFI sources can be suppressed to levels 168
 comparable to the level of Cas.A. The LOFAR RFI 169
 strategy is based on this assumption which is illustrated 170
 in Figure 1. The vertical scale represents radio wave flux 171
 levels and sensitivities in Jy. The curve “antenna sky 172

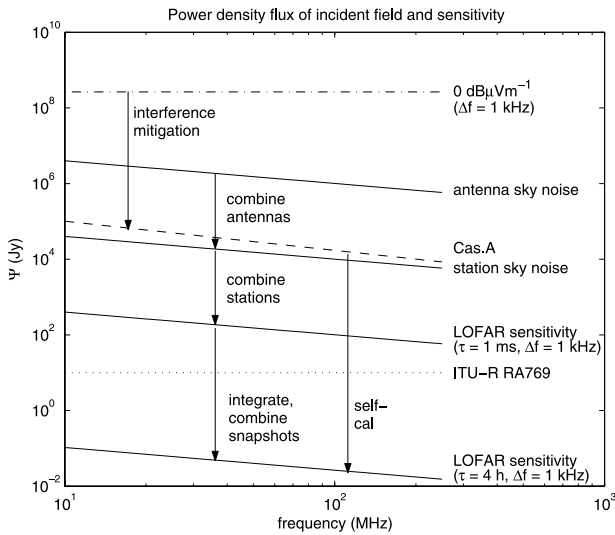


Figure 1. LOFAR sensitivity levels.

173 noise” shows the sky noise flux Ψ as a function
 174 of frequency, as would be observed with a single
 175 polarization LOFAR antenna dipole. It is based on the
 176 sky temperature, given by the approximate formula
 177 [Bregman, 2000; Kraus, 1986]

$$T_{sky} \approx T_{so} \lambda^{2.55} \text{ (K)} \quad (1)$$

179 and on a formula [Kraus, 1986; Rohlf, 1990] relating
 180 the sky temperature T_{sky} to the flux density Ψ

$$\Psi = 10^{26} \frac{2k}{\lambda^2} T_{sky} \Omega \text{ (Jy)} \quad (2)$$

182 Here Ω is the antenna solid angle (assumed to be 4 Sr), k
 183 the Boltzmann constant, and T_{so} is 60 ± 20 K for angular
 184 distances to the galactic plane larger than 10° .

185 [10] The dash-dotted curve in Figure 1 denotes a
 186 transmitter or interference flux level, and corresponds
 187 to a free space field strength of $0 \text{ dB}\mu\text{Vm}^{-1}$, assuming
 188 that the radio signal impinging on LOFAR is smeared out
 189 over a 1 kHz frequency channel width. At the LOFAR
 190 central core site in the Netherlands (above 30 MHz and
 191 outside the FM bands) nearly all transmitters and inter-
 192 ferers have observed powers less than $40 \text{ dB}\mu\text{Vm}^{-1}$.
 193 This was measured in a monitoring campaign; a large
 194 fraction of these transmitters even have observed powers
 195 below $0 \text{ dB}\mu\text{Vm}^{-1}$.

196 [11] In a station, (order) 100 antennae are combined in
 197 a phased array to form one or more beam(s). This means
 198 that the RMS noise level at the beam output is decreased
 199 by 20 dB and becomes approximately equal to the noise

power of Cas.A, one of the strongest sky sources. The
 200 RMS noise level at the beam output is represented by the
 201 curve “station sky noise” in Figure 1. It lies a few dBs
 202 below the “Cas.A” flux curve. 203

[12] In Figure 1, “LOFAR sensitivity” curves are
 204 drawn, both for 1 kHz bandwidth and for a synthesis
 205 array of (order) 100 stations. The two curves
 206 differ in integration time: 1 ms for the upper curve,
 207 and 4 h integration time for the bottom curve. 208
 209 Between the two LOFAR sensitivity curves, the
 210 (‘mean’) ITU-R RA769 emission criterion [International
 211 Telecommunication Union, 2003] is given, which
 212 roughly states the RFI level at which the error in
 213 determining the signal power exceeds 10% for an
 214 integration time of 2000 s. 215

2.3. LOFAR RFI Strategy 216

[13] The LOFAR RFI mitigation strategy is based on
 217 three steps. The first step in the strategy is choosing the
 218 optimum location for the LOFAR (order 200 kHz)
 219 subbands. Some of the 1 kHz bins in the 200 kHz bands
 220 may be affected by interference. In some cases, for
 221 example when a slight reduction of sensitivity is accept-
 222 able, these channels can be discarded, otherwise RFI
 223 mitigation measures need to be applied. 224

[14] The second step is reducing the RFI levels by RFI
 225 mitigation down to Cas.A power flux levels. These
 226 interference mitigation measures can be applied at station
 227 level before or after beam forming, or be applied at a
 228 central level, before or after correlation. Where this is
 229 optimally done in the signal chain is determined by
 230 various factors: the number of beam data bits, the data
 231 transport load, the number of correlator input bits, the
 232 linearity of the RFI Mitigation methods, etcetera. For
 233 LOFAR it was decided to apply only fixed or very
 234 slowly time-varying spatial nulls at station level. Fast
 235 changing interferer nulling directions would lead to fast
 236 changes in the (sidelobe) gains and this would hamper
 237 the calibration. Flagging or excising can best be done at a
 238 central level because interference often is localized. This
 239 means that interference may be present in one or a few
 240 stations, but not visible in an interferometer output. 241
 242 Flagging or excising at station level therefore often
 243 would remove too much data. The interference mitiga-
 244 tion measures in the second step will be applied at
 245 timescales up to 10 s.

[15] Step three is the reduction of interference from
 246 ‘Cas.A’ level down to sky image noise levels. This
 247 step is closely related to the map making process and
 248 involves long integration times. Removing (stationary)
 249 interferers should not be too different from removing
 250 sources such as Cas.A. In addition to Selfcal and
 251 Clean, other methods could be used [Leshem and
 252 van der Veen, 2000; Noordam, 2004]. Long-term and
 253 short-term stationarity issues as well as estimation
 254

255 biases [Leshem *et al.*, 2000; Raza *et al.*, 2002; van der
256 Tol and van der Veen, 2004] are relevant here and
257 require careful consideration.

258 [16] Two additional effects help reduce the observed
259 interference. The first is spectral dilution. Suppose that
260 in a LOFAR band a single narrowband RFI source is
261 present. The energy of this RFI source is diluted by
262 averaging all N_f frequency channels in the band. The
263 noise power decreases with $\sqrt{N_f}$, whereas the RFI
264 power decreases with N . This leads to a spectral
265 dilution factor which scales with $\sqrt{N_f}$. For wideband
266 signals such as CDMA (Code Division Multiple
267 Access, a signal coding scheme), this obviously does
268 not apply.

269 [17] A second effect which reduces interference is
270 spatial dilution. In the aperture synthesis mode, snapshot
271 images are made, and are integrated to form the inte-
272 grated map. Sky sources move with respect to the
273 baseline vectors during an observation. The interferers
274 on the other hand do not move, or move differently. This
275 means that in the integration process the sky sources
276 remain at the same sky positions and are ‘added’. The
277 RFI sources move with respect to the sky and
278 are therefore ‘diluted’. The dilution for an RFI point
279 source is comparable to the dilution of a narrowband
280 signal due to frequency averaging: the system noise
281 decreases with the square root of the number of snap-
282 shots whereas the RFI is reduced (as it moves around the
283 map) by the number of snapshots. This means that if
284 a point source is reduced to the station noise level, it will
285 be reduced to below the integrated noise level by further
286 integration (snapshot averaging). The spatial dilution is
287 the two-dimensional variant of fringe rotation, observed
288 in interferometers.

289 [18] On the basis of the analysis above and on
290 initial observations with ITS, it seems feasible that
291 the station sky noise level can be reached for certain
292 frequency ranges, even in densely populated regions
293 such as the Netherlands. With the help of Selfcal and
294 Clean type approaches, the remaining RFI can be
295 processed analogously to sources like Cas.A, and be
296 further reduced to levels at or below the integrated
297 sky noise.

299 3. Data Model

300 3.1. Received Data Model and Covariance Model

301 [19] In this section a single polarization point source
302 telescope signal model is described [Leshem *et al.*,
303 2000]. This model includes a description of astronom-
304 ical sources, additive interfering signals and noise.
305 Assume that there are p telescope antennae, and
306 suppose that the antenna signals $x_i(t)$ are composed
307 of q_s astronomical source signals, q_r interfering sour-

ces, and noise. Let the telescope output signals $x_i(t)$ be
stacked in a vector $\mathbf{x}(t)$ 308 309

$$\mathbf{x}(t) = (x_1(t), x_2(t), \dots, x_p(t))^t \quad (3)$$

[20] Further let $\mathbf{x}_\ell^s(t)$ be the telescope array output
signal corresponding to the ℓ th astronomical source in
the direction \mathbf{s}_ℓ , let $\mathbf{x}_k^r(t)$ be the telescope array output
signal corresponding to the k th interfering source in the
direction \mathbf{s}_k^r , and let $\mathbf{x}^n(t)$ be the noise vector. The
resulting array output signal then can be expressed by 317

$$\mathbf{x}(t) = \sum_{\ell=1}^{q_s} \mathbf{x}_\ell^s(t) + \sum_{k=1}^{q_r} \mathbf{x}_k^r(t) + \mathbf{x}^n(t) \quad (4)$$

[21] The noise $\mathbf{x}^n(t)$ is independent identically distrib-
uted (i.i.d.) Gaussian noise, so it is uncorrelated between
the array elements, or in other words spatially white at
the aperture plane. The astronomical source signals also
are assumed to be identically distributed Gaussian noise
signals. The sources are assumed to be independent, or in
other words spatially white at the celestial sphere. 326

[22] For the LOFAR ITS telescope experiments, we
assume that the narrowband interferer model [Leshem *et al.*,
2000; Whalen, 1971] holds. This means that for
narrowband signals with bandwidth Δf , the condition 330

$$\Delta f \ll \frac{1}{2\pi\tau} \quad (5)$$

is valid, where τ denotes the geometrical signal time
delay differences between the antenna elements. This
condition implies that geometric time delay differences
can be represented by phase shifts. For practical reasons,
the frequency resolution for the observations discussed
in this paper is 10 kHz, although the frequency resolution
of LOFAR will be of the order of 1 kHz. The maximum
geometric time delay across the array τ , is determined by
the array size (200 m) and observation direction. 340

[23] Assume that there is an interferer with index k ,
with signal $y_k^r(t)$. Because the narrowband condition
holds, the telescope output signal $\mathbf{x}_k^r(t)$ can be written
in terms of the array response vector \mathbf{A}_k^r . Let the array
response vector \mathbf{A}_k^r be defined by 345

$$\mathbf{A}_k^r = \begin{pmatrix} a_1^r e^{2\pi j \lambda^{-1} (\mathbf{B}_{10} \mathbf{s}_k^r)} \\ \vdots \\ a_p^r e^{2\pi j \lambda^{-1} (\mathbf{B}_{p0} \mathbf{s}_k^r)} \end{pmatrix} \quad (6)$$

where \mathbf{B}_{i0} is the location of the i th antenna with respect
to an arbitrary reference location, λ the wavelength of the 348

349 impinging signal, and a_i^r are the antenna gains in the
350 direction \mathbf{s}_k^r . This yields

$$\mathbf{x}_k^r(t) = \mathbf{A}_k^r y_k^r(t) \quad (7)$$

352 Let the antenna directional gain vector \mathbf{A}_k^{rg} be defined by
353 $\mathbf{A}_k^{rg} = (a_1^r, \dots, a_p^r)^t$, and define $\mathcal{R} = (\mathbf{B}_{10}, \dots, \mathbf{B}_{p0})^t$, then
354 \mathbf{A}_k^r can be compactly written as

$$\mathbf{A}_k^r = \mathbf{A}_k^{rg} \odot e^{\frac{2\pi}{\lambda} j \mathcal{R} \mathbf{s}_k^r} \quad (8)$$

356 Here the vector $e^{\frac{2\pi}{\lambda} j \mathcal{R} \mathbf{s}_k^r}$ represents the geometrical delay
357 (phase) vector for the telescope antenna locations \mathcal{R} and
358 the source direction \mathbf{s}_k^r .

359 [24] Assume there are q_r interferers, and define $\mathbf{x}^r(t)$ by
360 $\mathbf{x}^r(t) = \sum_k \mathbf{x}_k^r(t)$, which also can be written as

$$\mathbf{x}^r(t) = \sum_{k=1}^{q_r} \mathbf{A}_k^r y_k^r(t) \quad (9)$$

363 [25] The interferer signal power σ_k^2 is given by
364 $\mathcal{E}\{y_k^r(t)y_k^r(t)\} = \sigma_k^2$, which leads to the following expres-
365 sion for the interference array covariance matrix \mathbf{R}_r ,
366 dropping the time index t for \mathbf{R} :

$$\mathbf{R}_r = \mathcal{E}\{x^r(t)x^r(t)^H\} = \sum_{k=1}^{q_r} \sigma_k^2 \mathbf{A}_k^r (\mathbf{A}_k^r)^H \quad (10)$$

369 [26] The array response vector and the covariance
370 matrix \mathbf{R}_s for astronomical sources can be expressed in
371 a similar way. Concerning the system noise, it can be
372 represented by a diagonal noise matrix \mathbf{D} , and is given by

$$\mathbf{D} = \mathcal{E}\{\mathbf{x}^n(t)\mathbf{x}^n(t)^H\} = \text{diag}(\sigma_1^2, \dots, \sigma_p^2) \quad (11)$$

374 where the σ_i^2 is the noise power of the i th antenna
375 without source or interferer contributions.

376 [27] The covariance matrix

$$\mathbf{R} = \mathcal{E}\{\mathbf{x}(t)\mathbf{x}(t)^H\} \quad (12)$$

378 can be expressed as

$$\begin{aligned} \mathbf{R} &= \mathbf{R}_r + \mathbf{R}_s + \mathbf{D} \\ &= \sum_{k=1}^{q_r} \sigma_k^2 \mathbf{A}_k^r (\mathbf{A}_k^r)^H + \sum_{\ell=1}^{q_s} \sigma_\ell^2 \mathbf{A}_\ell^s (\mathbf{A}_\ell^s)^H + \mathbf{D} \end{aligned} \quad (13)$$

381 [28] Let \mathbf{A}_r be defined by stacking the array response
382 vectors for the interferers in a matrix

$$\mathbf{A}_r = [\mathbf{A}_1^r, \dots, \mathbf{A}_{q_r}^r] \quad (14)$$

and stack the interfering source powers in a diagonal
matrix \mathbf{B}_r . For the astronomical sources the same
definitions for \mathbf{A}_s and \mathbf{B}_s can be made. Using these
definitions, the covariance matrix \mathbf{R} can be expressed in
a more compact form:

$$\mathbf{R} = \mathbf{A}_r \mathbf{B}_r \mathbf{A}_r^H + \mathbf{A}_s \mathbf{B}_s \mathbf{A}_s^H + \mathbf{D} \quad (15)$$

3.2. Imaging and Beam Forming

[29] Traditionally [Perley *et al.*, 1994], the synthesized
sky images are generated by fourier transforming the
correlation data, here represented by the covariance
matrix \mathbf{R} . For the ITS station, the observed snapshots
contain only a fairly limited number of spatial sample
points. This implies that making sky images with the ITS
station using beam forming is more practical than using
spatial fourier transforms. Therefore the beam forming
approach, used for ITS imaging, is discussed next.

[30] Assume that the complex gain of the array antenna
elements can be adjusted by a multiplicative complex
weight number w_i for each of the antenna elements i .
Given the array output signal vector $\mathbf{x}(t)$ and a weight
vector for the array $\mathbf{w} = (w_1, \dots, w_p)^t$, then the weighted-
summed array output signal $y(t)$ is given by

$$y(t) = \mathbf{w}^H \mathbf{x}(t) \quad (16)$$

The beam former output power P is then given by

$$P = \mathcal{E}\{y(t)y(t)^H\} = \mathbf{w}^H \mathcal{E}\{x(t)x(t)^H\} \mathbf{w} = \mathbf{w}^H \mathbf{R} \mathbf{w} \quad (17)$$

[31] For a classical or capon beam former we can
define the weight vector, in terms of sky direction cosine
coordinates (l, m) :

$$\mathbf{w}^H(l, m) = \mathbf{A}^H(l, m) \quad (18)$$

where $\mathbf{A}(l, m)$ is the array response to signals from
direction (l, m) . The classical beam former is equivalent
to direct fourier transforming or taking the fourier
transform of all u, v data points without weighting.
The sidelobe pattern of this beam former is shown in
Figure 2.

4. Measurement Results

4.1. ITS Test Station

[32] The LOFAR ITS test station is located in the
northeast of the Netherlands. It is a sky noise limited
antenna array station consisting of $p = 60$ linearly
polarized antennae which are grouped in five spiral arms.
Each of the arms contain 12 single polarization inverted-

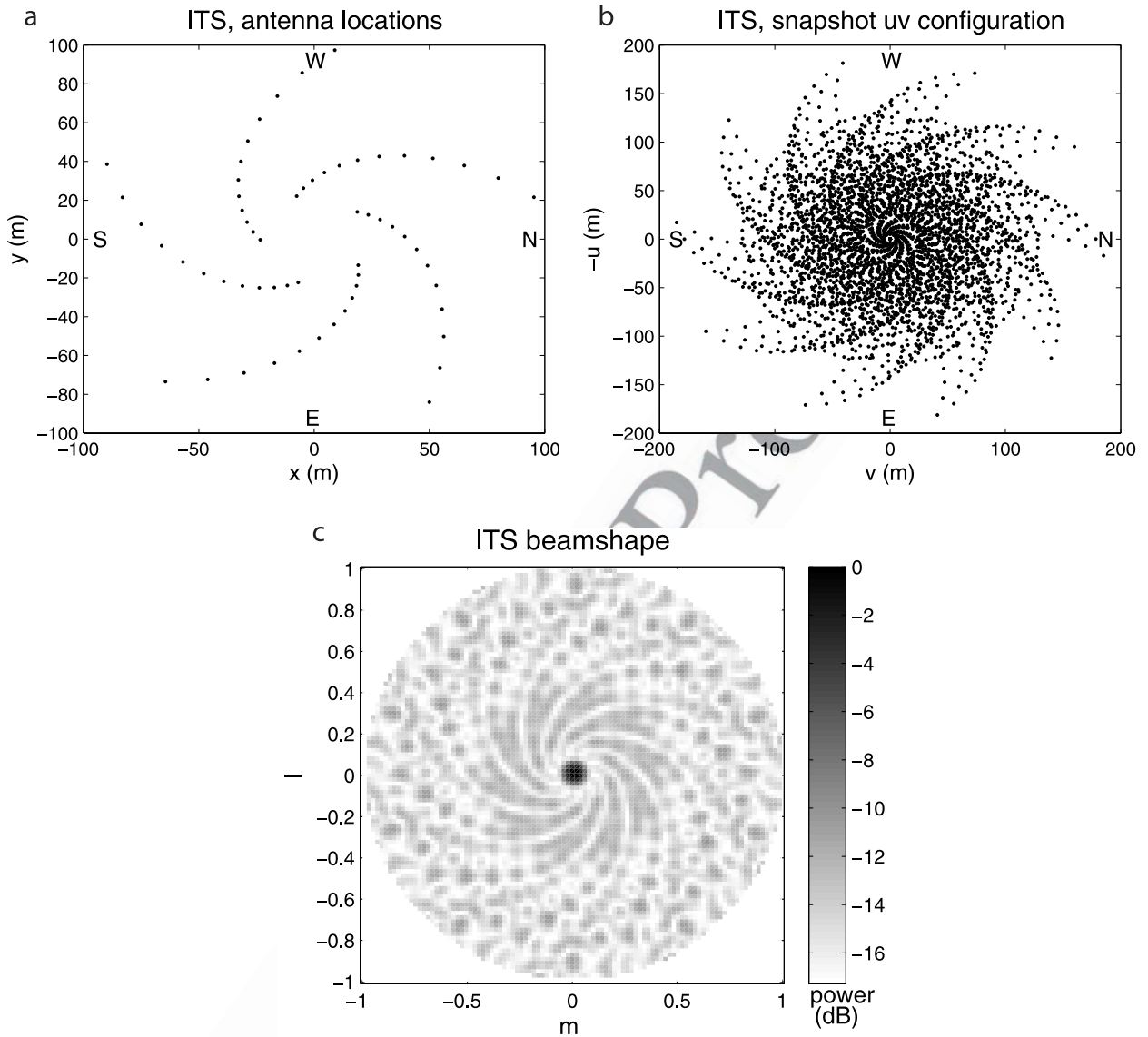


Figure 2. (a) LOFAR station ITS antenna configuration, (b) station snapshot (u, v) coverage, and (c) station beam shape when the beam is aimed in the zenith direction. The beam shape actually is the response to the entire hemisphere of sky (down to the horizon).

430 v dipoles with a resonance frequency of 34 MHz as can
 431 be seen in Figure 3. The dipoles are oriented in an east-
 432 west direction. The shortest antenna distance is 5 m,
 433 which corresponds to $\frac{1}{2}\lambda$ at 30 MHz. The diameter of the
 434 station is 200 m. The geometrical layout of the antenna
 435 locations is given in Figure 2a. A snapshot correlation
 436 measurement combines each of the antennae with all the
 437 others, yielding p^2 interferometer products. Each inter-
 438 ferometer product corresponds to a certain telescope

439 distance and direction, called baseline. Figure 2 (top
 440 right) shows the snapshot baseline configuration in a
 441 righthanded coordinate (u, v, w) system. Figure 2b shows
 442 the way in which the aperture is spatially sampled.
 443 Combining snapshot images will gradually fill the open
 444 spaces because the earth rotation changes the relative
 445 antenna positions with respect to the sky. Figure 2c
 446 shows the phased array beam shape at 30 MHz for the
 447 zenith direction. The beam width at this frequency is

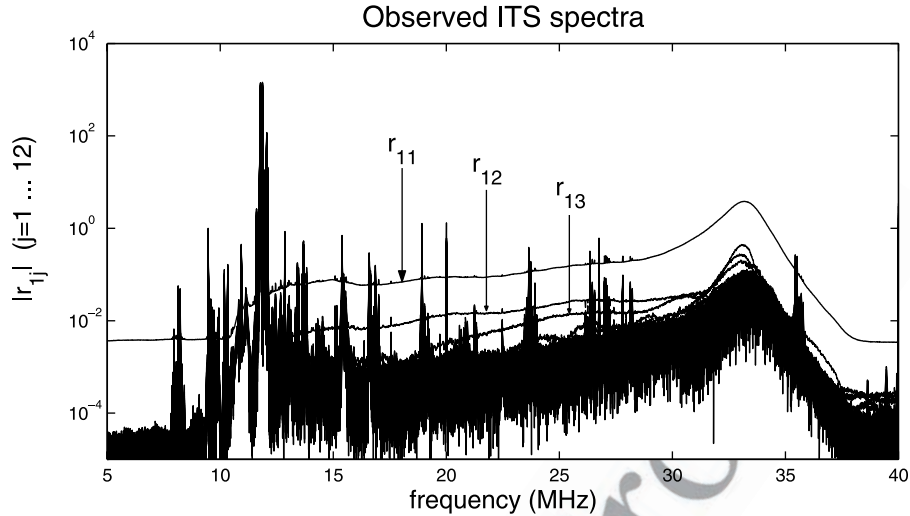


Figure 3. Nighttime ITS test station spectra of interferometers r_{1j} , with $j = 1 \dots 12$ and $\Delta f = 9.77$ kHz.

448 5.5° . The coordinates are direction cosines (l,m). The
449 north is defined in the positive m direction, the east in the
450 positive l direction.

451 [33] The antenna outputs are connected to low-noise
452 amplifiers, filtered by a 10–35 MHz filter, and digitized
453 with a sampling frequency of 80 MHz. For the experi-
454 ments described in this paper, a 8192 sample length,
455 Hanning tapered, FFT was used. This yielded a frequency
456 resolution of 9.77 kHz. The spectra were correlated
457 and integrated to 6.7 s, yielding a 60×60 covariance
458 matrix for each of the 4096 frequency bins. Figure 3
459 shows 12 observed interferometer spectra, of the inner
460 antenna of one of the arms, correlated with all antennae
461 in the same arm. Disconnecting an antenna and attaching
462 a matched load instead, reduces the observed autocorrela-
463 tion power \mathbf{R}_{11} by $\approx 75\%$, indicating that the sky noise
464 is the largest contributor to the system noise. Further
465 proof is given by *Wijnholds et al.* [2005], where it is
466 shown that the noise in the observed snapshot images is
467 dominated by the sky noise.

468 [34] Figure 3 also shows that the magnitudes of \mathbf{R}_{12} ,
469 \mathbf{R}_{13} , and \mathbf{R}_{14} are higher than those of the longer base-
470 lines. This is caused by the astronomical extended
471 sources in the sky, a well-known effect in aperture
472 synthesis [Kraus, 1986; Rohlfs, 1990; Perley et al.,
473 1994]. As the antennae closest to the center of the ITS
474 station (\mathbf{B}_{10} and \mathbf{B}_{20}) are only at a $\frac{1}{2}\lambda$ distance at 30 MHz,
475 there will be mutual coupling. This means that part of the
476 sky and receiver noise current in an antenna is coupled to
477 the other elements. In addition there could be electronic
478 coupling between receiver boxes, cabling etcetera.
479 Crosstalk would be best visible on the shortest antenna
480 spacings, making it difficult to distinguish it from ex-

tended astronomical sources. Method of moment antenna
481 simulations show however, that the crosstalk fraction
482 of the dipole at 40 MHz is -20 dB, and decreases to
483 -43 dB at 30 MHz and -65 dB at 20 MHz. This implies
484 that the cross talk can be ignored for most data process-
485 ing applications.

486
487 [35] The observed spectrum shows that a large fraction
488 of the 15–35 MHz band is sky noise limited at night, so
489 LOFAR observations could be carried out in those
490 frequency slots. By day the spectrum is more densely
491 occupied; an inventory of the occupancy statistics at ITS
492 is currently being carried out. The spectrum shows
493 harmonics and intermodulation products of strong trans-
494 mitters at 12 MHz. These signals appear at 24 and
495 36 MHz. As will be shown in the next sections, these
496 harmonics and intermodulation products can be sup-
497 pressed in the same way as “ordinary” transmitters.

4.2. Spatial Filtering

499
500 [36] Spatial filtering is demonstrated by applying pro-
501 jection filters and subtraction filters to the observed
502 covariance matrices $\hat{\mathbf{R}}$. These matrices $\hat{\mathbf{R}}$ are sample
503 estimates of \mathbf{R} and are constructed by

$$\hat{\mathbf{R}} = \frac{1}{N} \sum_{n=1}^N \mathbf{x}_n \mathbf{x}_n^H \quad (19)$$

506 [37] Here \mathbf{x}_n is the array signal output vector at time
507 index n; this index replaces the time variable t in
508 equation (4). We assume that model (15) is valid. As
509 we are investigating the suppression of relatively strong

510 interferers, we assume that the interferer power σ_k^2 is
 511 much larger than the astronomical sources power σ_s^2 . We
 512 further assume that the noise power matrix \mathbf{D} contains
 513 the spatially white sky noise which is dominant in
 514 strength. Now \mathbf{D} is initially unknown but it can be
 515 estimated for example with factor analysis approaches
 516 [Mardia *et al.*, 1979; Boonstra and van der Veen, 2003a,
 517 2003b]. Once \mathbf{D} is estimated, the matrix $\hat{\mathbf{R}}$ can be
 518 whitened, for example by premultiplying and postmulti-
 519 plying it with $\hat{\mathbf{D}}^{-\frac{1}{2}}$. The whitening process also affects
 520 $\hat{\mathbf{R}}_s$, but this can be corrected after filtering. Consider now
 521 the following simplified whitened model

$$\mathbf{R} = \mathbf{A}_r \mathbf{B}_r \mathbf{A}_r^H + \mathbf{R}_s + \sigma_n^2 \mathbf{I} \quad (20)$$

523 where we assume that the interferer power is dominant.
 524 This model will be used further to explain the working of
 525 the spatial filters.

526 4.2.1. Projection Filtering

527 [38] The covariance matrix \mathbf{R} can be filtered using
 528 projection matrices [Leshem *et al.*, 2000]. As before, let
 529 \mathbf{A}_k^r be a matrix containing the interferer array response
 530 vectors \mathbf{A}_k^r , and assume that \mathbf{A}_k^r is known. Define the
 531 projection matrix \mathbf{P} by

$$\mathbf{P} = \mathbf{I} - \mathbf{A}_r (\mathbf{A}_r^H \mathbf{A}_r)^{-1} \mathbf{A}_r^H \quad (21)$$

533 Because $\mathbf{P} \mathbf{A}_r = \mathbf{0}$, pre and post multiplying \mathbf{R} with \mathbf{P}
 534 yields for the filtered covariance matrix $\check{\mathbf{R}}_{\perp}$:

$$\check{\mathbf{R}}_{\perp} = \hat{\mathbf{R}} \mathbf{P} \quad (22)$$

$$\mathcal{E}\{\check{\mathbf{R}}_{\perp}\} = \mathbf{P} (\mathbf{R}_s + \sigma_n^2 \mathbf{I}) \mathbf{P} \quad (23)$$

538 The interference is removed, but the astronomical
 539 sources are distorted by the filter. This distortion can
 540 be removed by approaches such as described by Leshem
 541 *et al.* [2000], Raza *et al.* [2002], and van der Tol and van
 542 der Veen [2004], but it is beyond the scope of this paper
 543 to apply these techniques here.

544 4.2.2. Subtraction Filtering

545 [39] An alternative filtering method is interference
 546 subtraction. With known σ_n^2 , \mathbf{B}_r , and \mathbf{A}_r , or their esti-
 547 mates, the contribution of the interferer can be reduced
 548 by subtracting it from the observed covariance matrix.
 549 Let $\check{\mathbf{R}}_{-}$ be the filtered covariance matrix, that is the
 550 observed covariance matrix with the estimated interfer-
 551 ence removed by subtraction, then:

$$\check{\mathbf{R}}_{-} = \hat{\mathbf{R}} - \mathbf{A}_r \mathbf{B}_r \mathbf{A}_r^H \quad (24)$$

$$\mathcal{E}\{\check{\mathbf{R}}_{-}\} = \mathbf{R}_s + \sigma_n^2 \mathbf{I} \quad (25)$$

4.2.3. Attenuation Limits and Subspace Analysis 556

557 [40] When the spatial signature of the interferers and
 558 its power is unknown, it can be estimated by an eigena-
 559 nalysis of the sample covariance matrix $\hat{\mathbf{R}}$. Because of
 560 limits in the estimation accuracies, both filter types will
 561 have estimation errors and may also be biased [Leshem
 562 and van der Veen, 2000]. In some case the bias can be
 563 corrected [van der Tol and van der Veen, 2004].
 564 These estimation errors will not be discussed in
 565 detail here. Now we will briefly describe how to
 566 estimate the interferer parameters using a subspace
 567 analysis. The covariance matrix \mathbf{R} can be written in
 568 terms of eigenvalues and eigenvectors as [Leshem *et*
 569 *al.*, 2000]

$$\mathbf{R} = \mathbf{U} \mathbf{\Lambda} \mathbf{U}^H \quad (26)$$

571 where \mathbf{U} is a unitary matrix containing the eigenvectors,
 572 and $\mathbf{\Lambda}$ is a diagonal matrix containing the eigenvalues.
 573 Assuming that the astronomical contribution is so small
 574 it can be ignored, with the exception of the extended
 575 spatially white emission, the eigenvalue decomposition
 576 can be expressed as

$$\mathbf{R} = [\mathbf{U}_r \mathbf{U}_n] \begin{bmatrix} \mathbf{\Lambda}_r + \sigma_n^2 \mathbf{I}_{q_r} & \mathbf{0} \\ \mathbf{0} & \sigma_n^2 \mathbf{I}_{p-q_r} \end{bmatrix} \begin{bmatrix} \mathbf{U}_r^H \\ \mathbf{U}_n^H \end{bmatrix} \quad (27)$$

578 where \mathbf{U}_r is a $p \times q_r$ matrix, containing the eigenvectors
 579 corresponding to the q_r eigenvalues in $\mathbf{\Lambda}_r$. \mathbf{U}_n is a $p \times p$
 580 matrix containing the eigenvectors, corresponding to the
 581 noise subspace. Given a matrix \mathbf{R} , the signal subspace
 582 can be found by applying a singular value decomposition
 583 to \mathbf{R} . Note that the signal subspace and the noise
 584 subspace span the entire space, $\mathbf{U} = [\mathbf{U}_r \mathbf{U}_n]$, and \mathbf{U} is
 585 unitary: $\mathbf{U} \mathbf{U}^H = \mathbf{U}_s \mathbf{U}_s^H + \mathbf{U}_n \mathbf{U}_n^H = \mathbf{I}_p$. Without further
 586 knowledge, the best estimate of \mathbf{A}_r is the dominant
 587 eigenspace \mathbf{U}_r of $\hat{\mathbf{R}}$, and likewise the best estimate of the
 588 interferer powers \mathbf{B}_r is $\mathbf{\Lambda}_r - \sigma_n^2 \mathbf{I}$.

589 4.2.4. Experimental Results

590 [41] Figure 4 shows the eigenvalue structure of $\hat{\mathbf{R}}$
 591 of the nighttime observation discussed earlier. The eigen-
 592 value decomposition was applied after a whitening step.
 593 The largest eigenvalue of the observed transmitter at
 594 25.752 MHz lies 20 dB above the remaining eigenval-
 595 ues. This means that the observed transmitter power lies
 596 20 dB above the sky noise level, and that the transmitter
 597 occupies (for at least 99% of its power) only one
 598 dimension of the subspace of $\hat{\mathbf{R}}$. Therefore we have
 599 chosen to base the spatial filters on one direction
 600 vector only, namely the one corresponding to the largest
 601 eigenvalue.

602 [42] Figure 5a, shows the results of the beam former
 603 scan over the entire sky of the data set of 26 February

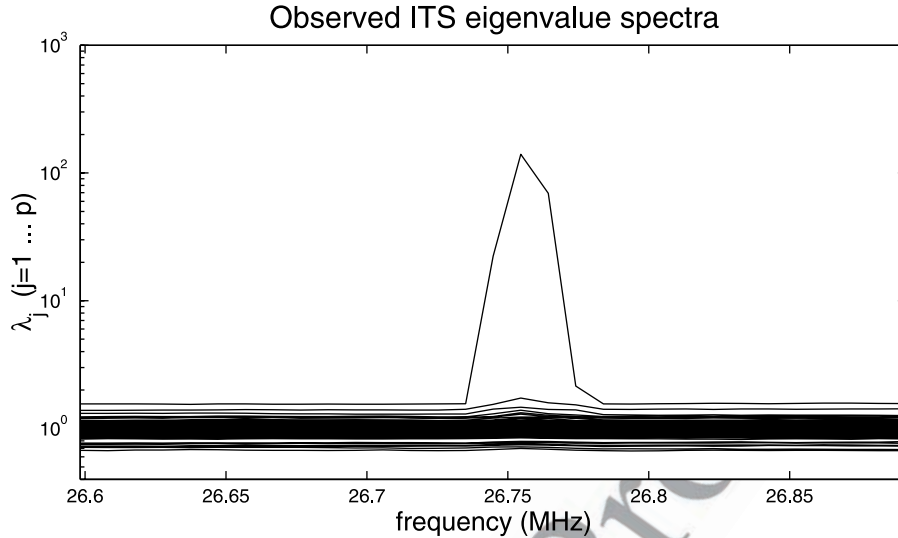


Figure 4. Eigenvalue distribution for $N_{sam} = 131,000$, $\Delta t = 6.7$ s, $\Delta f = 9.77$ kHz, measured on 26 February 2004.

2004, at 03:50 MET. The sky is shown at a single frequency bin at 26.89 MHz; no interference or transmitters were detected. The astronomical sources Cas.A (to the right of the image), and Cyg.A (near the top of the image) are clearly visible. An extended structure, the “north galactic spur” is just visible as a band from $(m,l) = (-0.6, -0.2)$ to $(m,l) = (-0.3, 0.9)$. Figure 5b is a sky image from the same data set, but now at 26.75 MHz in which a transmitter was detected. It is visible at the horizon at $(l,m) = (0.45, -0.9)$. It is 20 dB above the noise (cf. Figure 4), and its sidelobes spread around the map and obscure the astronomical sources. In Figure 5c, the same map is shown, but now it is improved by applying a projection filter. In this experiment, the distortion correction, discussed earlier, was not applied. Clearly, sidelobe structure residuals of the uncorrected projection filter distort the map more than the subtraction filter which is shown in Figure 5d. This, however, does not imply that subtraction filters are better than projection filters, as the projection filter was uncorrected. The point here is that spatial filtering can attenuate a transmitter 20 to 30 dB above the sky noise to levels below the Cas.A flux level. At 18.92 MHz we showed (not displayed here), the same for a transmitter 30 dB above the sky noise level. The residual transmitter sidelobes were also suppressed to levels below Cas.A.

4.2.5. Detection of RFI Using Eigenvalue Decomposition

[43] As a further illustration of the relation between the eigenstructure of the observed covariance matrices and the number of detectable interfering sources, we show

two examples in Figure 6. Figure 6a shows an eigenvalue distribution with one dominant largest eigenvalue and one dominant source in accompanying the map. Figure 6b shows three dominant eigenvalues and three interfering sources in the map.

4.3. Intermodulation Products

[44] The purpose of the following analysis is to show that intermodulation products appear as additional point sources in the map. The consequence of this is that these sources can be mitigated just like ordinary sources and that spatial dilution is also applicable for these sources.

[45] Intermodulation products are caused by nonlinearities in the receiver, often caused by high-power transmitter signals distorting the low-noise amplifier linearity. Assume that the transmitter signals are semi-stationary. For a simple second-order model of the amplifier and given input signal $x(t)$, the output $y(t)$ is given by

$$y(t) = \beta_1 x(t) + \beta_2 x^2(t) \quad (28)$$

where β_1 and β_2 are two real parameters describing the (non)linearity behavior. Let us consider the scenario where the input consists of the sum of two cosines with different amplitude (α_1, α_2), frequency (f_1, f_2) and phase (θ_1, θ_2)

$$x(t) = \alpha_1 \cos(2\pi f_1 t + \theta_1) + \alpha_2 \cos(2\pi f_2 t + \theta_2) \quad (29)$$

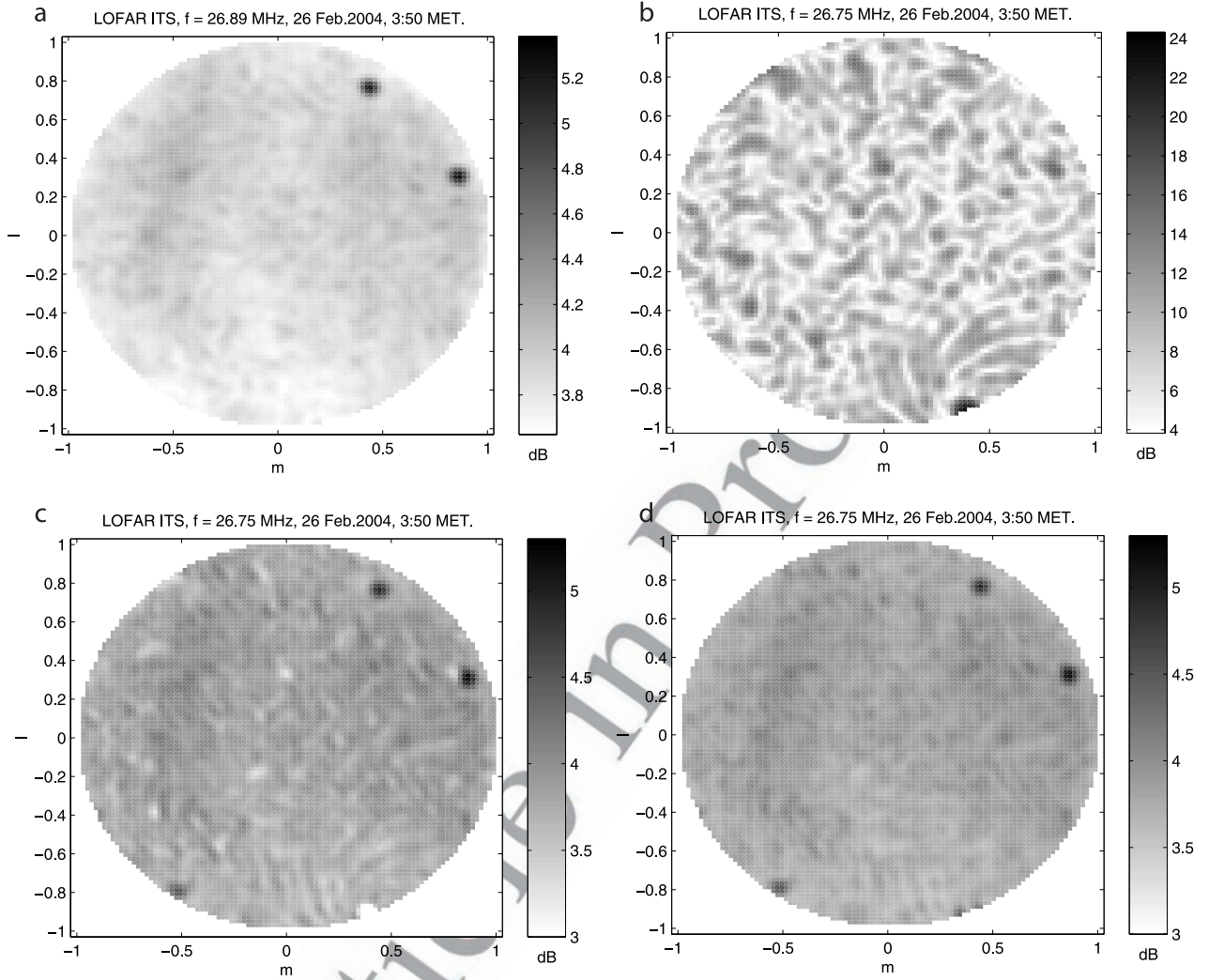


Figure 5. Spatial filtering at LOFAR ITS test station: (a) snapshot image without interference at 26.89 MHz, (b) snapshot image with a transmitter at 26.75 MHz, (c) image with transmission removed by spatial filtering using a projection filter, and (d) image with transmission removed by spatial filtering using a subtraction filter.

661 the output of the amplifier is then given by

$$\begin{aligned}
 y(t) = & \beta_1 \alpha_1 \cos(2\pi f_1 t + \theta_1) + \beta_1 \alpha_2 \cos(2\pi f_2 t + \theta_2) \\
 & + \beta_2 \alpha_1^2 / 2 (1 + \cos(2\pi 2f_1 t + 2\theta_1)) \\
 & + \beta_2 \alpha_2^2 / 2 (1 + \cos(2\pi 2f_2 t + 2\theta_2)) \\
 & + \beta_2 \alpha_1 \alpha_2 \cos(2\pi(f_1 + f_2)t + \theta_1 + \theta_2) \\
 & + \beta_2 \alpha_1 \alpha_2 \cos(2\pi(f_1 - f_2)t + \theta_1 - \theta_2)
 \end{aligned} \quad (30)$$

663 The first two terms are wanted, the last four are
664 intermodulation products.

[46] Now consider two cosine signals impinging on an
665 array of antennae. The sum of these two cosines can be
666 modeled as
667

$$\begin{aligned}
 \mathbf{x}(t) = & \alpha_1 \odot \cos(2\pi f_1 t \mathbf{1} + \boldsymbol{\theta}_1) \\
 & + \alpha_2 \odot \cos(2\pi f_2 t \mathbf{1} + \boldsymbol{\theta}_2)
 \end{aligned} \quad (31)$$

669 where α_k is the vector containing the real signal
670 amplitudes, and $\boldsymbol{\theta}_k$ is the antenna phase vector of
671 the k th transmitter. The phase vector $\boldsymbol{\theta}_k$ can be expressed
672 in terms of geometric telescope positions $\mathcal{R} = (\mathbf{B}_{10}, \dots, \mathbf{B}_{72})$

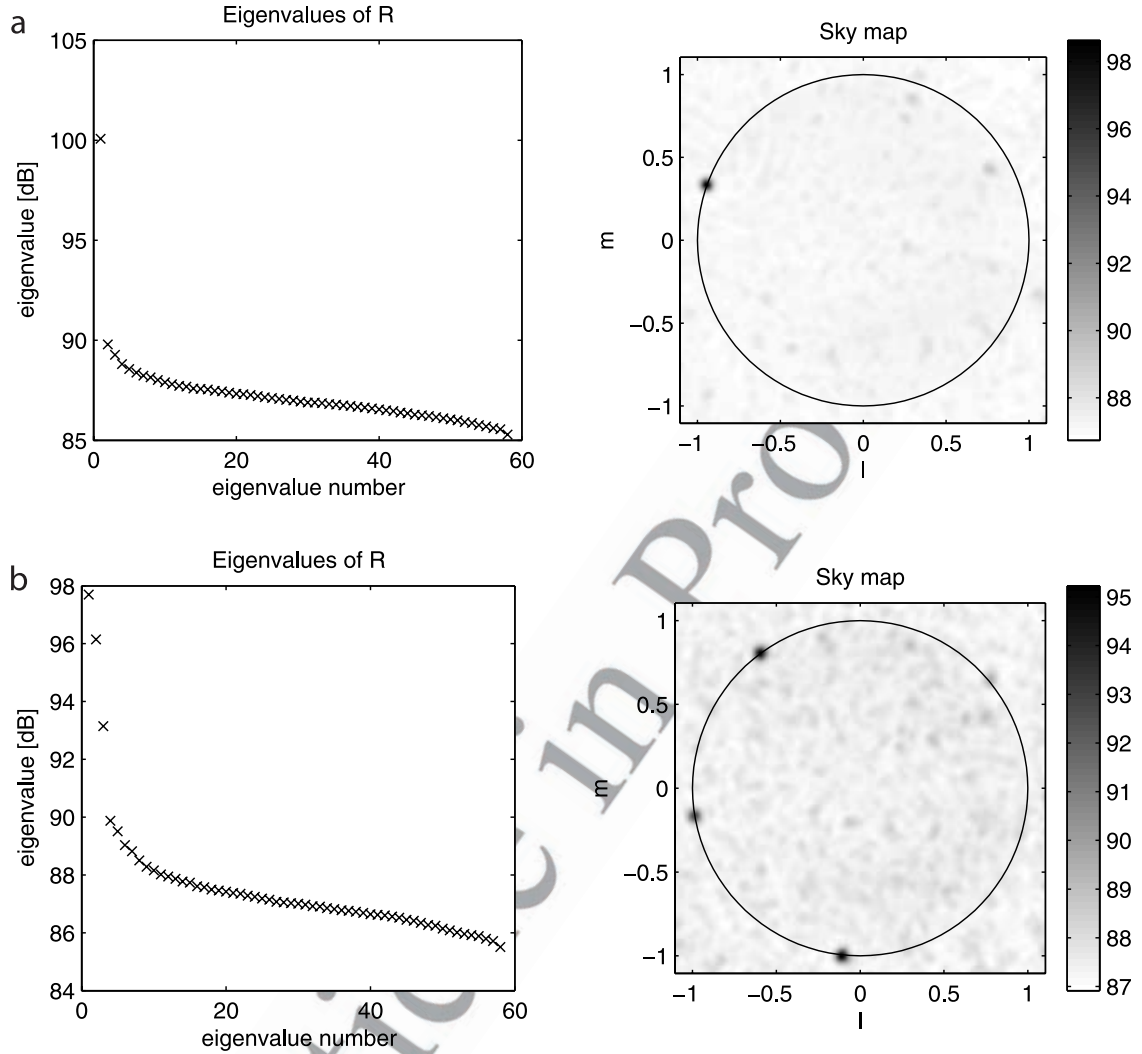


Figure 6. Eigenvalue decomposition of covariance matrices and celestial maps from the LOFAR initial test station. Shown are observations at (a) 27.800 and (b) 27.096 MHz. There is a clear correlation between the number of observed strong sources and the number of large eigenvalues.

673 \mathbf{B}_{p0}^t , wavelength λ_k and the source direction \mathbf{s}_k of the k th
 674 transmitter

$$\boldsymbol{\theta}_k = \frac{2\pi}{\lambda_k} \mathcal{R} \mathbf{s}_k \quad (32)$$

676 The transmitter source direction vector \mathbf{s}_k is a unit norm
 677 vector.

$$\mathbf{s}_k \equiv \begin{bmatrix} l \\ m \\ n \end{bmatrix} \quad (33)$$

Table 1. Predicted Directions in (l,m) Coordinates of Transmitters and Their Intermodulation Products as They Will Appear in Celestial Maps

f	l	m	t1.2
f_1	l_1	m_1	t1.3
f_2	l_2	m_2	t1.4
$2f_1$	l_1	m_1	t1.5
$2f_2$	l_2	m_2	t1.6
$f_1 + f_2$	$\frac{\lambda_2 l_1 + \lambda_1 l_2}{\lambda_1 + \lambda_2}$	$\frac{\lambda_2 m_1 + \lambda_1 m_2}{\lambda_1 + \lambda_2}$	t1.7
$f_1 - f_2$	$\frac{\lambda_2 l_1 - \lambda_1 l_2}{\lambda_1 - \lambda_2}$	$\frac{\lambda_2 m_1 - \lambda_1 m_2}{\lambda_1 - \lambda_2}$	t1.8

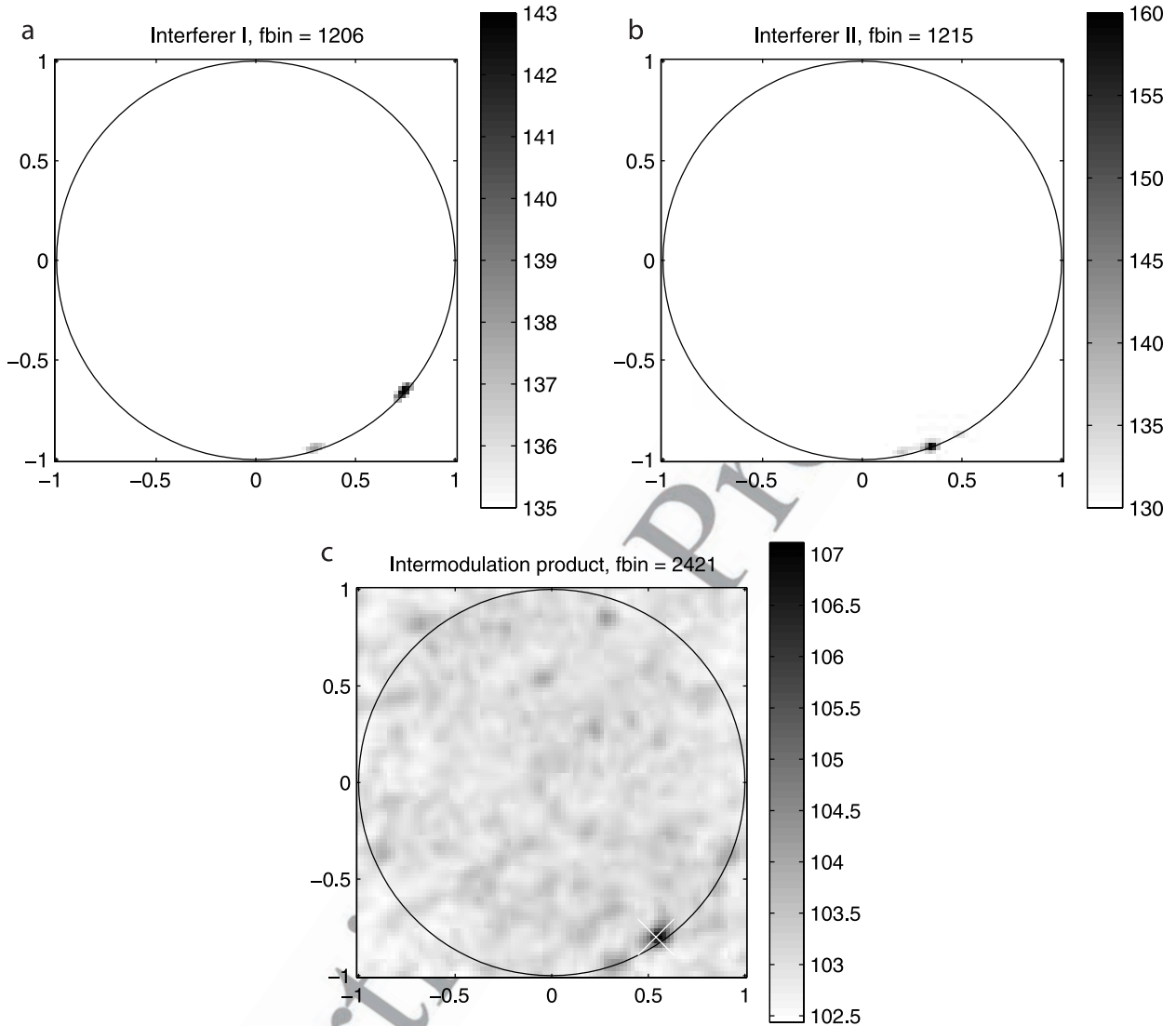


Figure 7. Two strong interfering point sources are visible at the horizon at (a) 11.77 and (b) 11.86 MHz. (c) The summed frequency intermodulation product is visible at a location in between the two “parent” sources. The intermodulation product is marked with a cross and remains a point source.

679 [47] To specify a location only two coordinates (l, m)
 680 are necessary, the third coordinate is chosen such that
 681 the vector unit norm. For a planar array in the x,y
 682 plane the z coordinate of the antenna positions is zero.
 683 All items of the third column of \mathcal{R} are zero, which
 684 means that the phase θ is independent of the third
 685 component of \mathbf{s}_k .

686 [48] The sum of two cosines with frequencies f_1 and f_2
 687 at the input gives the sum of six cosines with frequencies
 688 $f_1, f_2, 2f_1, 2f_2, f_1 + f_2$ and $f_1 - f_2$. Let us consider the

intermodulation response $\mathbf{y}_i(t)$ at $f_{i2} = f_1 + f_2$ in more 689
 detail 690

$$\mathbf{y}_i(t) = \beta_2 \odot \alpha_1 \odot \alpha_2 \odot \cos(2\pi(f_1 + f_2)t\mathbf{1} + \theta_1 + \theta_2) \quad (34)$$

where β_2 is the vector containing the second-order 692
 nonlinearity parameters for each of the antennae. 693

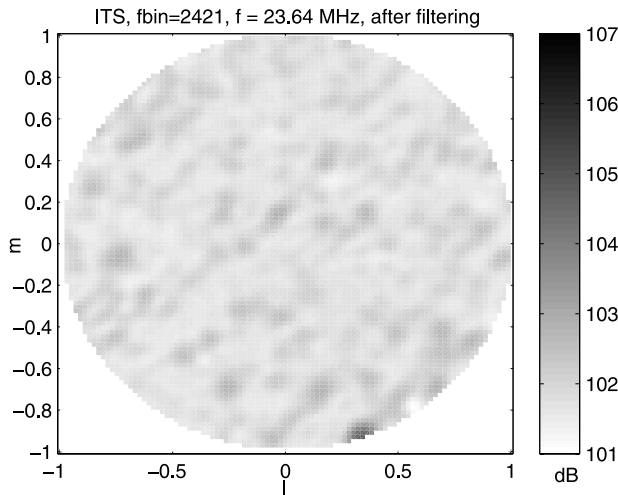


Figure 8. Sky map showing the effect of a rank-1 spatial projection filter on an intermodulation product. The intermodulation product, a point source, is suppressed by at least 10 dB.

694 The sum of the phases $\theta_1 + \theta_2$ can be expressed
695 by

$$\begin{aligned}\theta_1 + \theta_2 &= \frac{2\pi}{\lambda_1} \mathcal{R} \mathbf{s}_1 + \frac{2\pi}{\lambda_2} \mathcal{R} \mathbf{s}_2 \\ &= 2\pi \mathcal{R} \left(\frac{\mathbf{s}_1}{\lambda_1} + \frac{\mathbf{s}_2}{\lambda_2} \right)\end{aligned}\quad (35)$$

698 [49] Suppose there exists a real source (i.e., not an
699 intermodulation product) at frequency $f_{12} = f_1 + f_2$, or
700 wavelength λ_{12}

$$\lambda_{12} = \frac{\lambda_1 \lambda_2}{\lambda_1 + \lambda_2}\quad (36)$$

701 and suppose this source has a direction given by

$$\mathbf{s}_{12} = \frac{\lambda_2 \mathbf{s}_1 + \lambda_1 \mathbf{s}_2}{\lambda_1 + \lambda_2}\quad (37)$$

703 Then this source will have the following phases

$$\begin{aligned}\theta &= \frac{2\pi}{\lambda_{12}} \mathcal{R} \mathbf{s}_{12} \\ &= 2\pi \mathcal{R} \frac{\lambda_1 + \lambda_2}{\lambda_1 \lambda_2} \frac{\lambda_2 \mathbf{s}_1 + \lambda_1 \mathbf{s}_2}{\lambda_1 + \lambda_2} \\ &= 2\pi \mathcal{R} \left(\frac{\mathbf{s}_1}{\lambda_1} + \frac{\mathbf{s}_2}{\lambda_2} \right)\end{aligned}\quad (38)$$

706 These phases are equal to the phases of the intermodulation
707 product described earlier, which means that the
708 intermodulation product will appear as a point source in

the map in the weighted direction \mathbf{s}_{12} . The direction 709
vector \mathbf{s}_{12} is not unit norm, but there does exist a 710
vector with the same (l, m) and a different n 711
coordinate which is unit norm. Since for a planar 712
array the phases do not depend on the n coordinate, a 713
signal from this direction has the same phases as the 714
intermodulation product. The absolute value of the 715
spatial signature is different. 716

[50] So we can conclude that intermodulation products 717
appear as additional sources in the image at predictable 718
positions as given in Table 1. As the nonlinearity 719
variation over the array differs from the antenna (side- 720
lobe) gain variation over the array, in principle we can 721
distinguish intermodulation products from real sources. 722

[51] Figure 7 shows an ITS observation with strong 723
interferers at 11.77 MHz and 11.86 MHz. The intermodulation 724
product consisting of the sum of the two signals 725
appears exactly at the predicted location, indicated by the 726
white cross. Figure 8 shows the same data set, but shown 727
after application of a spatial projection filter. The inter- 728
modulation product clearly is removed by the rank-1 729
filter. What remains are nearby (multipath?) sources, 730
which can be removed as well by increasing the rank 731
or subspace of the projection filter. 732

4.4. Minimum Variance Distortionless Response and Robust Capon Beam Forming

[52] The weights of the classical beam former are 736
independent of the data. The image quality can be 737
improved by using a data-dependent beam former. Min- 738
imum variance distortionless response (MVDR) beam 739
forming [Madisetti and Williams, 1998; Van Trees, 2002] 740
gives a significant suppression of the sidelobes compared 741
to classical beam forming. The MVDR beam former 742
minimizes the output power under the constraint that the 743
gain in the desired direction remains unity: 744

$$\mathbf{w}_{\text{MVDR}}(l, m) = \arg \min_{\mathbf{w}} \mathbf{w}(l, m)^H \mathbf{R} \mathbf{w}(l, m)\quad (39)$$

with the constraint

$$\mathbf{w}_{\text{MVDR}}(l, m)^H \mathbf{A}(l, m) = 1\quad (40)$$

The solution to this equation can be found using 748
Lagrange multipliers, and is given by 749

$$\mathbf{w}_{\text{MVDR}}(l, m) = \frac{\mathbf{R}^{-1} \mathbf{A}(l, m)}{\mathbf{A}(l, m)^H \mathbf{R}^{-1} \mathbf{A}(l, m)}\quad (41)$$

The measured intensity is given by

$$I(l, m) = \frac{1}{\mathbf{A}(l, m)^H \mathbf{R}^{-1} \mathbf{A}(l, m)}\quad (42)$$

The MVDR beam former is known to be sensitive to 753
array calibration errors, leading to errors in the beam 754

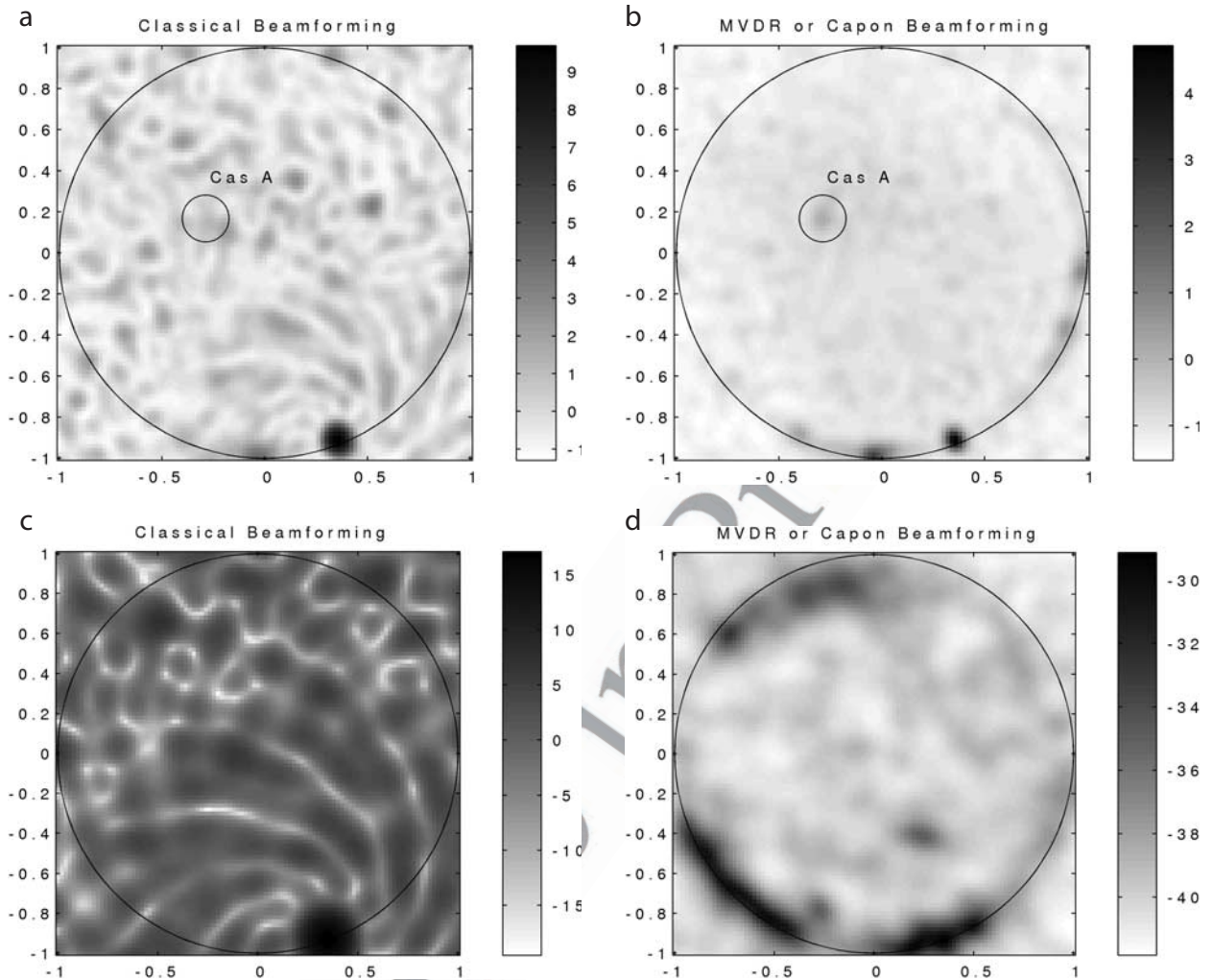


Figure 9. Celestial daytime maps obtained with the LOFAR test station using the MVDR beam former and the classical beam former. (a–b) Shown are Cas.A and a transmitter at the horizon at 11.86 MHz and 9.77 kHz bandwidth. (c–d) Shown are the same results, but at a nearby frequency with a more dominant transmitter.

755 gain. More robust versions of MVDR exist such as
 756 robust capon beam forming [Stoica *et al.*, 2003], but
 757 these are not discussed in detail here.
 758 [53] Spatially filtered data in the sky maps can be
 759 corrected using space varying beams [Leshem *et al.*,
 760 2000]. MVDR and robust capon beam formers can be
 761 extended to include such operations. Figure 9 shows
 762 illustrations of the use of a classical beam former and an
 763 MVDR beam former to produce “dirty” images. The top
 764 images show that an MVDR beam former has a much
 765 sharper beam than compared to the classical beam
 766 former, and a much smoother sidelobe structure. In this

daytime observation, the classical beam former does not
 767 reveal the strong source Cas.A; the MVDR beam former
 768 does show the source. A drawback of MVDR is that
 769 calibration errors can cause the MVDR beam former to
 770 underestimate the power. Especially the higher peaks can
 771 be strongly diminished by this effect, resulting in a lower
 772 dynamic range. A clear example of this effect is shown in
 773 Figures 9c and 9d. The difference in dynamic range is
 774 more than 20 dB. In literature, methods have been
 775 proposed to improve the performance of the MVDR
 776 beam former for arrays with imperfect calibration. We
 777 have chosen the robust capon beam forming method of
 778

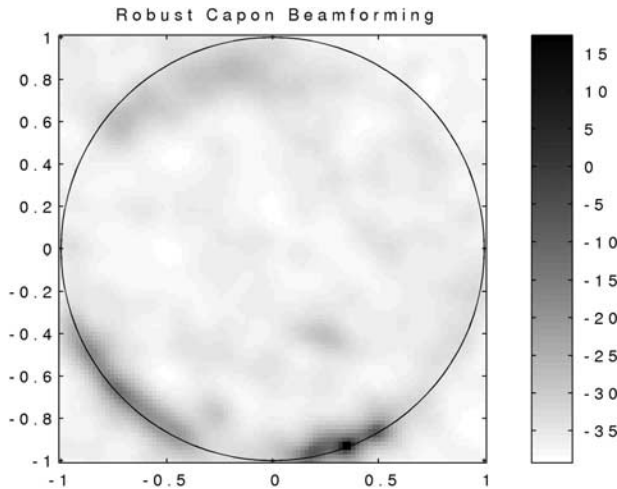


Figure 10. Celestial map obtained with the LOFAR test station using the robust capon beam former. The image shows the sky at 11.86 MHz and at a bandwidth of 9.77 kHz. A strong interfering source is visible at the bottom right horizon; a band of interfering signals is visible at the bottom left horizon. Cas.A and the galactic plane are not visible.

779 Li, Stoica, and Wang as proposed by *Stoica et al.* [2003].
 780 The result of this method is shown in Figure 10. The
 781 intensity scaling (array/beam gain) is restored. The
 782 observed beam width is very small, which suggests that
 783 robust capon beam forming could enhance some of the
 784 calibration approaches in the astronomical imaging pro-
 785 cess. This, however, needs further study.

787 5. Conclusions

788 [54] In this paper we have demonstrated spatial filter-
 789 ing capabilities at the LOFAR initial test station (ITS),
 790 and have related it to the LOFAR RFI mitigation
 791 strategy. We have shown that with ITS, in frequency
 792 ranges which are occupied with moderate-intensity in-
 793 terfering signals, the strongest astronomical sky sources
 794 can be recovered by spatial filtering. The same Selfcal
 795 and Clean approaches which remove the sidelobe struc-
 796 tures of the strongest sources such as Cas.A can also be
 797 used to mitigate the interference further. The spatial
 798 dilution effect helps reducing the interference. We have
 799 also shown that intermodulation products originating
 800 from point sources remain point sources and can be
 801 attenuated with the same spatial filtering techniques as
 802 nonintermodulation interference. We have shown and
 803 verified experimentally that even the direction of an
 804 intermodulation product can be predicted. Finally, we
 805 have demonstrated the use of several beam former types
 806 for ITS.

References

- Barnbaum, C., and R. F. Bradley (1998), A new approach to 808
 interference excision in radio astronomy: Real-time adaptive 809
 cancellation, *Astron. J.*, 115, 2598–2614. 810
- Boonstra, A. J. (2002), RFI mitigation strategy, *Rep. LOFAR-*
ASTRON-DOC-004, Low Frequency Array, Dwingeloo, 811
 Netherlands. 812
- Boonstra, A. J., and A. J. van der Veen (2003a), Dual polariza- 814
 tion gain estimation for radio telescope arrays, paper pre- 815
 sented at IEEE International Conference on Acoustics, 816
 Speech, and Signal Processing (ICASSP), Inst. of Electr. 817
 and Electron. Eng., Hong Kong, April. 818
- Boonstra, A. J., and A. J. van der Veen (2003b), Gain calibra- 819
 tion methods for radio telescope arrays, *IEEE Trans. Acoust.*
Speech Signal Process., 51(1), 25–38. 820
- Bregman, J. D. (2000), Concept design for a low frequency 822
 array, in *Radio Telescopes, Proc. SPIE*, vol. 4015, edited 823
 by H. R. Butcher, pp. 19–32, Int. Soc. for Opt. Eng., Bel- 824
 lingham, Wash. 825
- Briggs, F. H., J. F. Bell, and M. J. Kesteven (2000), Removing 826
 radio interference from contaminated astronomical spectra 827
 using an independent reference signal and closure relations, 828
Astron. J., 120, 3351–3361. 829
- Ellingson, S. W., J. D. Bunton, and J. F. Bell (2001), Removal 830
 of the GLONASS C/A signal from OH spectral line obser- 831
 vations using a parametric modelling technique, *Astrophys.*
J. Suppl. Ser., 135(1), 87–93. 833
- Fridman, P. A., and W. A. Baan (2001), RFI mitigation 834
 methods in radio astronomy, *Astron. Astrophys.*, 378,
 327–344. 836
- International Telecommunication Union (2003), Protection cri- 837
 teria used for radio astronomical measurements, in *Recom-*
mendation ITU-R RA.769-1, Geneva, Switzerland. 839
- Kollen, H. (2004), LOFAR system requirements specification, 840
Rep. LOFAR-ASTRON-SRS-001, Low Frequency Array,
 Dwingeloo, Netherlands, May. 842
- Kraus, J. D. (1986), *Radio Astronomy*, 2nd ed., McGraw-Hill, 843
 New York. 844
- Leshem, A., and A. J. van der Veen (2000), The effect of 845
 adaptive interference suppression on radio astronomical 846
 image formation, in *Radio Telescopes, Proc. SPIE*, vol. 847
 4015, edited by H. R. Butcher, pp. 341–352, Int. Soc. for 848
 Opt. Eng., Bellingham, Wash. 849
- Leshem, A., A. J. van der Veen, and A. J. Boonstra (2000), 850
 Multichannel interference mitigation techniques in radio 851
 astronomy, *Astrophys. J. Suppl. Ser.*, 131(1), 355–373. 852
- Madisetti, V. K., and D. B. Williams (Eds.) (1998), *The Digital* 853
Signal Processing Handbook, Electr. Eng. Handbook Ser.,
 CRC Press, Boca Raton, Fla. 855
- Mardia, K. V., J. T. Kent, and J. M. Bibby (1979), *Multivariate* 856
Analysis, Probab. Math. Stat., Elsevier, New York. 857
- Noordam, J. E. N. (2002), Generalized self-calibration for 858
 LOFAR, paper presented at 27th General Assembly of the 859
 International Union of Radio Science, Maastricht, Nether- 860
 lands, Aug. 861

- 862 Noordam, J. E. N. (2004), LOFAR calibration challenges, paper
863 presented at SPIE Conference on Astronomical Telescopes
864 and Instrumentation, Int. Soc. for Opt. Eng., Glasgow, U. K.,
865 June.
- 866 Perley, R. A., F. R. Schwab, and A. H. Bridle (1994), *Synthesis*
867 *Imaging in Radio Astronomy*, *Astron. Soc. Pac. Conf. Ser.*,
868 vol. 6, Astron. Soc. of the Pac., San Francisco, Calif.
- 869 Raimond, E., and R. Genee (Eds.) (1996), *The Westerbork Ob-*
870 *servatory, Continuing Adventure in Radio Astronomy*, *Astro-*
871 *phys. Space Libr.*, vol. 207, Springer, New York.
- 872 Raza, J., A. J. Boonstra, and A. J. van der Veen (2002), Spatial
873 filtering of RF interference in radio astronomy, *IEEE Signal*
874 *Process. Lett.*, 9, 64–67.
- 875 Rohlfs, K. (1990), *Tools of Radio Astronomy*, Springer, New
876 York.
- 877 Stoica, P., Z. Wang, and J. Li (2003), Robust capon beamform-
878 ing, *IEEE Signal Process. Lett.*, 10, 172–175.
- 879 Thompson, A. R., J. R. Moran, and G. W. Swenson (1986),
880 *Interferometry and Synthesis in Radio Astronomy*, 1st ed.,
881 John Wiley, Hoboken, N. J.
- van der Tol, S. V., and A. J. van der Veen (2004), Performance
analysis of spatial filtering of RF interference in radio
astronomy, *IEEE Trans. Acoust. Speech Signal Process.*,
53, 896–910.
- Van Trees, H. L. (2002), *Detection, Estimation, and Modula-*
tion Theory, part 4, *Optimum Array Processing*, Wiley-
Interscience, Hoboken, N. J.
- Whalen, A. D. (1971), *Detection of Signals in Noise*, Elsevier,
New York.
- Wijnholds, S. J., J. D. Bregman, and A. J. Boonstra (2005), Sky
noise limited snapshot imaging in the presence of RFI with
the LOFAR initial test station, *Exp. Astron.*, in press.
-
- A. J. Boonstra, Research and Development Department,
ASTRON, Oude Hoogeveensedijk 4, NL-7991 PD Dwingeloo,
Netherlands. (boonstra@astron.nl)
- S. van der Tol, Department of Electrical Engineering, Delft
University of Technology, Mekelweg 4, NL-2628 CD Delft,
Netherlands. (svdt@cas.et.tudelft.nl)